AIMS Materials Science

AIMS Materials Science, 12(6): 1296–1317.
DOI: 10.3934/matersci.2025060
Received: 23 October 2025
Revised: 21 November 2025
Accepted: 03 December 2025
Published: 15 December 2025

https://www.aimspress.com/journal/Materials

Research article

The effect of the shielding environment on the structure and content of the main alloying elements during laser melting of Al-Mg and Al-Zn-Mg-Cu aluminum alloys by fiber laser irradiation

Volodymyr Korzhyk[1,2,*], Oleksandr Babych[1,2], Xinxin Wang[1], Vladyslav Khaskin[2,*], Sviatoslav Peleshenko[1], Alla Chaika[2], Andrii Aloshyn[2], Yunqiang Zhao[1,*], Guirong[2] and Yanchao Hu[2]

[1] China-Ukraine Institute of Welding, Guangdong Academy of Sciences, Guangdong Provincial Key Laboratory of Material Joining and Advanced Manufacturing, Guangzhou, 510650, China

[2] E.O. Paton Electric Welding Institute, National Academy of Sciences of Ukraine/11 Kazymyr Malevych Str., Kyiv, 03150, Ukraine

* **Correspondence:** Email: vnkorzhyk@gmail.com; khaskin1969@gmail.com; zhaoyq@gwi.gd.cn; Tel: +3-80-973-119-263.

Abstract: The influence of argon shielding configurations for the weld pool on microstructure formation and the retention of principal alloying elements during partial penetration of Al-Mg and Al-Zn-Mg-Cu alloys using fiber laser irradiation at a power of 900 W with a specific energy input of 100–130 J/mm was analyzed. The studies were conducted under the following conditions: (1) in an open chamber with local argon shielding; (2) in a sealed chamber filled with argon (pressure 1.05 MPa); (3) in the same chamber with additional argon flow onto the weld pool (flow rate 5–10 L/min); (4) in a sealed chamber with reduced argon pressure (170–190 Pa); and (5) in the same chamber with additional argon flow onto the weld pool (flow rate 5–10 L/min). For shielding schemes No. 1–No. 3, penetration depths of 0.20–0.23 mm were achieved. Application of schemes No. 4 and No. 5, as opposed to scheme No. 1, led to a reduction in oxide inclusions in the penetration cross-section from 3.0% to 1.5% or lower, which complied with ISO 13919-2:2001. However, this was accompanied by a decrease in the proportion of alloying elements, particularly Mg, Zn, and Cu, to 50%–70% or more, and a 10%–30% reduction in microhardness of the fusion zone relative to the base metal. The use of scheme No. 5 promoted a transition in penetration mode from heat conduction to deep penetration, accompanied by an increase in penetration depth up to five-fold and a reduction in alloying

element burn-off. Laser penetration of the studied alloys was carried out in heat conduction mode. The regime promoted vertical crystallite growth, whereas in the deep penetration mode, transcrystallite counter-growth of crystallites at an angle to the central penetration zone was observed.

Keywords: laser welding; aluminum alloys; shielding gas configurations of the bath; structure; microhardness; content of alloying elements

1. Introduction

Aluminum alloys are the primary structural material traditionally used for the fabrication of rocket and aircraft components in aviation and aerospace structures [1–3]. To maintain the advantages of these alloys in the manufacture of welded aerospace products, it is essential to take into account such aspects of their weldability as the structural and chemical heterogeneity of the weld metal and heat-affected zone, crack resistance, and mechanical properties [4–7]. To comprehensively understand the characteristic features of structure formation, a series of studies was carried out using thermal impact analysis and mathematical modeling [8–11].

A notable feature of welding aluminum alloys is their high affinity for oxygen, which leads to the potential formation of an oxide film (Al_2O_3) in the welds [12–15], as well as their high thermal conductivity, which complicates the development of various fusion welding technologies for these alloys [16–19].

In the welding of thin-walled structures, it is possible to enhance mechanical properties through the deliberate modification of the structure, which can be achieved by employing welding with a concentrated heat source to localize the thermal effect on the base metal [20–23]. For the welding of critical thin-walled structures, electron beam and plasma welding are commonly used [24,25].

The weldability challenges of aluminum alloys underscore the importance of investigating their behavior under concentrated heat sources [26,27]. For instance, alloys of the Al-Mg and Al-Zn-Mg-Cu systems exhibit low technological weldability due to their pronounced tendency toward crack formation, high coefficients of linear thermal expansion, and low evaporation temperatures of alloying elements, particularly Zn and Mg [28–31]. This contributes to the formation of welding defects such as cracks [32–35]. However, modern technologies enable the successful welding of alloys previously considered difficult to weld, for example, by laser fusion welding using a high-power density heat source [36–39].

Owing to its high energy concentration, laser welding is one method for reducing the influence of high thermal conductivity on the formation of significant residual stresses and deformations in welded structures [40–43]. It can ensure the formation of high-quality joints with minimal residual stresses and deformations [44,45]. However, laser welding of aluminum alloys presents certain technological challenges [46–49]. Thus, the presence of a dense oxide film on the edges of aluminum alloys to be welded requires thorough surface preparation (cleaning), and the high reflectivity and thermal conductivity of aluminum can diminish the efficiency of laser radiation absorption, resulting in reduced melting depth [50–52].

Therefore, the use of laser welding of aluminum alloys opens new possibilities for producing high-quality and durable welded joints in aerospace products [53–55]. In such cases, challenges may

arise when welding with a non-penetrating seam; for example, when welding is the final operation and elimination of spatter from the root zone of the melt is required. Such challenges can be addressed either through laser welding in the heat conduction penetration mode or in the deep (keyhole) penetration mode, which exhibits high stability of penetration depth. In all cases, the formation of high-quality penetrations requires the establishment of a reliable gas shielding atmosphere for the weld pool. This study is dedicated to investigating these issues.

Our objective of this study is to investigate the effect of various weld pool gas shielding configurations during laser melting of aluminum alloys in the Al-Mg and Al-Zn-Mg-Cu systems on microstructure formation and variation of the major alloying element contents in the remelted metal, as well as to determine the regularities of their structure formation.

2. Materials and methods

For the experimental investigations, samples were prepared from alloys of the Al-Mg (5052, 5083) and Al-Zn-Mg-Cu (7064) systems (Table 1). These materials were selected as models to simulate real aerospace products that require precision hermetic joints. Alloys 5052 and 5083 exhibit high strength and corrosion resistance, are easily formable at room temperature, and demonstrate good weldability. They are widely used in the production of aviation equipment, boats, household appliances, and automotive components. Alloy 7064 is a high-strength wrought alloy. It is characterized by high strength, rigidity, and good workability under pressure, which promotes its use in various industries, particularly in aerospace engineering for the fabrication of load-bearing structures and fuselage components.

Table 1. Chemical composition of the experimental samples (wt.%) [56].

Registered international designation/system	Si	Fe	Cu	Mn	Mg	Cr	Zn	Ti	Zr	Others		Al
										Each	Total	
5052/Al-Mg	≤0.25	≤0.4	≤0.1	≤0.1	2.2–2.8	0.15–0.35	≤0.1	–	–	0.05	0.15	Base
5083/Al-Mg	≤0.4	≤0.4	≤0.1	0.4–1.0	4–4.9	0.05–0.25	≤0.25	≤0.15	–	0.05	0.15	Base
7064/Al-Zn-Mg-Cu	≤0.12	≤0.15	1.8–2.4	–	1.9–2.9	0.06–0.25	6.8–8.0	–	0.1–0.5	0.05	0.15	Base

The study was conducted according to the following methodology. Partial penetration melting was performed in plates measuring 50 × 50 × δ mm, where the thickness δ = 4 and 5 mm, using laser irradiation in different shielding environments with the following five argon gas shielding configurations for the weld pool:

(1) In air (in an open chamber) with local shielding of the weld pool by argon (flow rate 25 L/min).

(2) In an argon atmosphere within a sealed chamber, which was filled with argon following evacuation (pressure 1.05 MPa).

(3) The same, with additional argon purging of the weld pool (flow rate 5–10 L/min).

(4) In a sealed chamber under an argon atmosphere at reduced pressure (170–190 Pa).

(5) The same, with additional argon purging of the weld pool (flow rate 5–10 L/min).

During the research, the reliability of the gas shielding of the weld pool was determined by the following basic requirements, corresponding to ISO 13919-2:2001: In the remelted weld metal, the

maximum total size of oxide inclusions should not exceed 3% of the cross-sectional area of the melt, while the thickness of the oxide film should be no more than 0.01 mm. The experiments were carried out according to the scheme presented in Figure 1. To determine the dimensions of the penetration cross-section, statistical data were collected by performing measurements on three cross-sections of different samples with subsequent averaging of the obtained data.

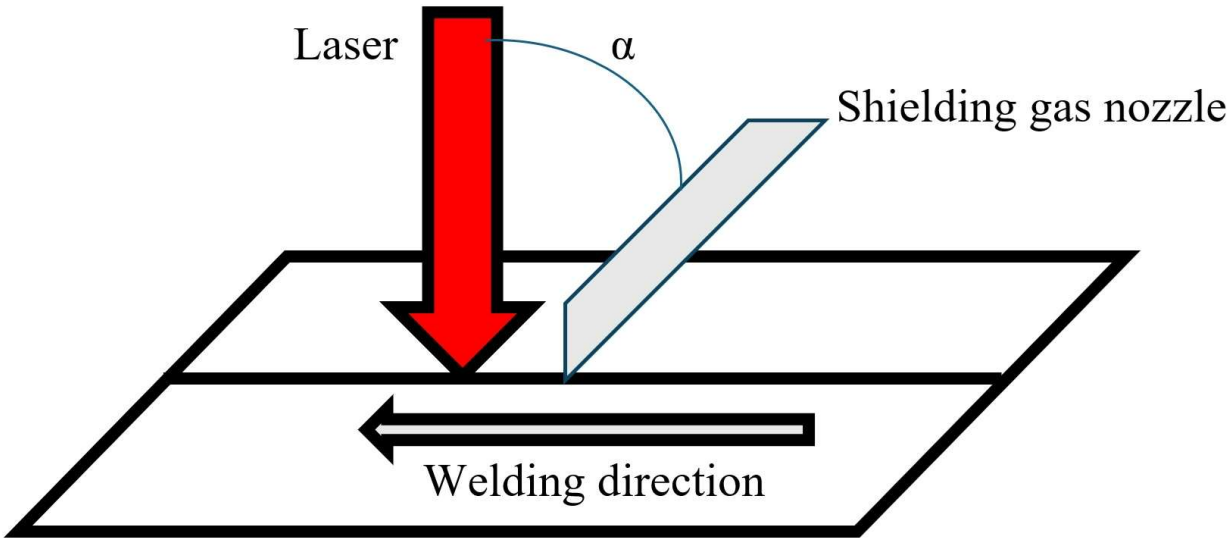

Figure 1. Scheme of laser welding experiments (angle of inclination of the shielding gas supply nozzle α = 45º; the depth of the focus relative to the surface of the welded sample is 10 mm).

To reliably achieve non-through melting, the laser welding process was performed in the so-called heat conduction mode. In this welding mode, the surface of the weld pool exhibited minimal depression and no keyhole was formed, unlike welding in deep penetration mode. Typically, heat conduction mode is not employed in laser welding due to a significant decrease in process efficiency. However, in this study, this regime was selected to more distinctly demonstrate the influence of gas shielding configurations on the formation of the laser melting. To attain the heat conduction mode of laser welding, the focus of the fiber laser radiation was positioned at least 10 mm below the surface of the specimen.

Cross-sectional macro- and microsections were prepared from the obtained melted samples [57,58], which were subsequently used for metallographic studies of the geometric and structural parameters of the penetrations, as well as their chemical composition [59–62]. For this purpose, the structural constituents on the polished sections were revealed by electrolytic etching in a solution of glacial acetic and chloric acids. Microhardness measurements were performed using a Leco M-400 microhardness tester (LECO, USA). Metallographic studies were conducted using a Neophot 32 optical microscope (CARL ZEISS Jena, Germany) and a Tescan Mira 3 LMU scanning electron microscope equipped with an Oxford Instruments Inca Energy energy-dispersive spectrometer and an X-Max 80 detector (TESCAN, Czech Republic) [63–65]. Comprehensive material analysis methods were applied for all other investigations [66–69].

3. Results

The experiments were conducted using specially developed pilot-scale equipment, which enabled welding in air with local protection of the weld pool, as well as in a controlled atmosphere, including under reduced pressure. The equipment consisted of the following major components (Figure 2): 1: hermetic welding chamber with manipulator for rotating and moving the specimens; 2: inlet assembly with coordinate adjustment system for the welding head; 3: gas preparation system with equipment for regulating the pressure in the chamber; 4: recirculating gas system with equipment for supplying, circulating, and cooling inert gases (argon, helium); 5: fixture for securing the specimens being welded; 6: laser welding head; 7: technological fiber laser, model MFSC-1000 (Maxphotonics, China), with a power output up to 1 kW and a wavelength of 1070 nm; 8: equipment control system with a programmable PLC controller; 9: temperature control system including a pyrometer for non-contact monitoring of heating during welding.

Figure 2. External view of the technological complex and vacuum chamber with a rotary manipulator for welding in a protective controlled atmosphere at various pressures.

A hermetically sealed welding chamber equipped with a manipulator for rotating and moving the samples to be welded enabled operations both in a low-pressure atmosphere (10^0–10^1 Pa) and in an inert gas atmosphere (argon, helium) when the chamber is filled (Figure 2). The working pressure in the chamber during laser melting experiments was 1.05 MPa when the chamber was filled with argon, and 170–190 Pa under low-pressure atmospheric conditions. The sample for welding was mounted in

the manipulator (rotation mechanism) using specialized equipment. The chamber was equipped with systems for visual monitoring of the welding processes and non-contact temperature measurement of the sample by a pyrometer, as well as units for inert gas delivery and gas blowing of the weld pool. To eliminate the negative impact of laser optics contamination on the stability of weld formation, a cross-jet with argon purging at a flow rate of 10 L/min was installed under the window to input focused laser radiation into the welding chamber.

Immediately prior to conducting laser welding studies, the sample surfaces were prepared to remove the oxide film by mechanical (scraping) or chemical (etching in NaOH alkali and HNO_3 acid) methods. During the study, five selected weld pool gas shielding schemes were sequentially employed.

Welding was performed in automatic mode at a speed of 25 m/h, with a laser power of 900 W and a focal depth set at 10 mm below the surface of the sample undergoing melting. The linear welding energy input in all cases was 100–130 J/mm [70]. During specimen rotation, a continuous ring-shaped weld was formed (Figure 3). The closure was performed with a gradual decrease in laser power; however, the closure zone (5–10 mm in length) was not considered in subsequent studies. The criterion for selecting the melting regime for the specimen was that its heating did not exceed 100 °C. Upon completion of the laser melting process, the specimen was removed from the chamber and the equipment was prepared for the next experiment.

Figure 3. External appearance of laser melt pools in alloy 5083 (δ = 5 mm): (a) on the abraded surface; (b) on the etched surface.

The selected regime, with intentional defocusing by 10 mm when using the first three gas shielding schemes, provided the so-called heat conductive laser melting mode [71–74], which is characterized by slight sagging of the weld pool surface and a weld shape factor K > 1 (K = W/D, where W is the weld width and D is its depth) [75–77]. When the fifth shielding gas configuration was employed, the melting regime shifted from heat conductive to deep (keyhole), which is characterized by the formation of a vapor-gas channel (keyhole) and a weld shape coefficient K ≤ 1. In this case, the penetration depth increased up to five times. The transition to the deep penetration regime was

facilitated by argon flow (5–10 L/min) directed onto the weld pool at an angle of up to 45º relative to the axis of the focused laser beam under reduced pressure conditions (170–190 Pa). It should be noted that under either normal or elevated pressure (1.05 MPa), with an analogous argon shielding gas flow over the weld pool, the transition to deep melting was not observed. This effect can be explained by the enhancement of metal vapor dispersion under reduced pressure, which is typically generated above the weld pool. This results in a substantial reduction of the laser-induced plasma plume and improves the depression of molten metal under the pressure of the argon jet, which, in turn, facilitates keyhole formation under laser irradiation [78–80].

4. Discussion

The sample preparation stage for laser melting demonstrated the following. It was established that, in the case of scraped samples, weld formation was non-uniform, exhibiting significant fluctuations in the width and depth of penetration, and the repeatability of the results was unsatisfactory (Figure 3a). In contrast, for melted etched samples, weld formation was stable with satisfactory repeatability of results (Figure 3b). The described results were observed regardless of the ambient pressure. Studies have shown that during scraping of the samples, particles of the Al_2O_3 oxide film entered the metal and contributed to increased absorption of laser radiation by the surface, which led to an increase in the width and depth of melting. In contrast, areas of the sample surfaces that lacked Al_2O_3 particles or contained them in insignificant amounts absorbed laser radiation less efficiently, resulting in a decrease in the width and depth of melting.

As a result of the described studies, it was determined that, to achieve stable depth and width of laser melting, it is necessary to ensure optical uniformity in radiation absorption by the welded surface. In the case of aluminum alloys, this is achieved by replacing preliminary scraping of the welded edges with chemical etching, which prevents the introduction of oxide scale fragments into the metal that would otherwise significantly increase radiation absorption. Therefore, only chemical etching was used to prepare samples for subsequent experiments.

When investigating the effect of the shielding environment on microstructure formation and changes in the content of the major alloying elements in the remelted metal during laser welding, attention was given to the formation of the weld cross-section and the corresponding crystallite growth directions, weld microhardness, as well as the tendency for changes in the content of alloying elements with the lowest evaporation temperatures, namely Zn and Mg.

An analysis of the cross-sectional formation of the weld revealed the following findings (Table 2): laser welding in a dynamic low-pressure atmosphere with weld pool blowing results in approximately a fivefold increase in penetration depth, accompanied by a 20%–30% increase in weld width compared to all other gas shielding configurations. Laser welding in an argon atmosphere within a sealed chamber, combined with weld pool blowing, results in an increase in weld width of up to 15%, while the penetration depth remains virtually unchanged. All other shielding gas configurations have virtually no effect on changes in the cross-sectional shape of the laser melt pools.

Table 2. Major geometrical parameters of laser melt pools in aluminum alloy 7064 (δ = 4 mm), produced using the investigated shielding gas configurations.

Shielding gas configuration No.	Macrosection of penetration	Penetration depth (H), mm	Penetration width (L), mm
1	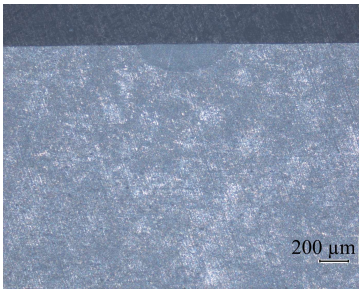	0.21	0.7
2	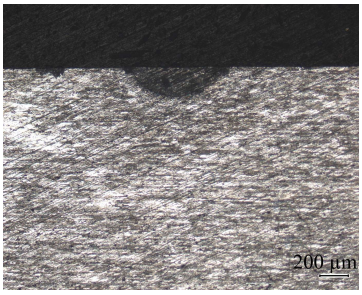	0.23	0.7
3	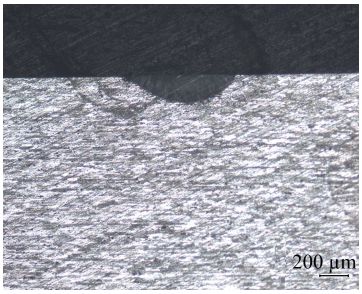	0.2	0.8
4	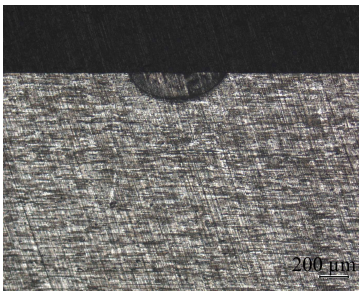	0.2	0.7
5	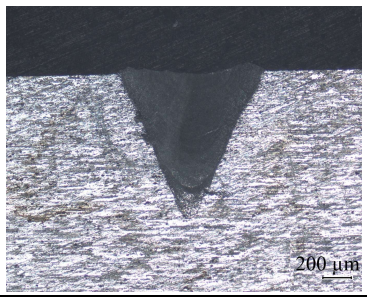	1.0	1.0

It should be noted that for laser melting according to schemes 1–4 (Table 2), the cross-sectional area of remelted metal in the seams is approximately 0.100–0.101 mm^2, while for melting according to scheme 5 it is 0.5 mm^2. Therefore, the specific energy density for melting according to schemes 1–4

is 8900–9000 J/mm^2, and for melting according to scheme 5 it is 1800 J/mm^2. Therefore, reducing the ambient gas pressure while simultaneously purging the weld pool with an inert gas (argon) enables a fivefold decrease in the specific energy density required to achieve melting in the 7064 alloy. As further experiments have demonstrated, this trend remains consistent for all the aluminum alloys investigated.

The investigation of oxide formation in the metal of laser melts was conducted using metallographic methods. In all cases, the maximum size of oxide inclusions did not exceed 3% of the fusion cross-sectional area, and the thickness of the oxide film was no greater than 0.002 mm. This corresponds to the requirements of ISO 13919-2:2001 [81]. The research data indicated that when shielding gas configuration No. 1 was employed, the greatest quantity of oxide inclusions was observed; up to 3% of the fusion cross-sectional area (Figure 4a). When using shielding gas configuration No. 2, the amount of these inclusions decreases to 1.5%–2.0%. The smallest fraction of these oxide inclusions (less than 1.5% of the penetration cross-sectional area) was observed with shielding gas configurations No. 4 and No. 5 (Figure 4b).

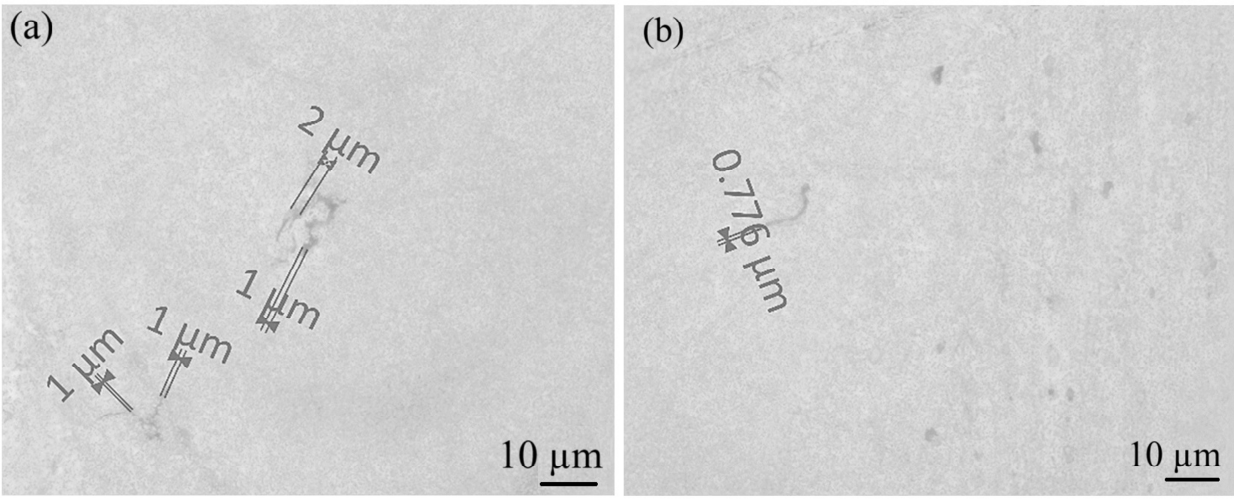

Figure 4. Al_2O_3 oxide film inclusions in the metal of laser melt pools in 5083 alloy (δ = 5 mm) under gas shielding: (a) configuration No. 1; (b) configuration No. 5.

Microhardness analysis of laser melt pools formed under various shielding environments indicated that, for alloys 5052 and 5083, modifications in the shielding gas configurations of the weld pool exert a negligible effect on this parameter (Figure 5). The obtained results fall within the measurement error and the standard deviation of HV0.1 microhardness values for these alloys [82,83]. To a greater extent, variations in shielding gas configuration impact the high-strength alloy 7064. The greatest hardness (comparable to that of the base metal) is observed when employing the first of the studied configurations (in air with local argon shielding of the weld pool), which can be attributed to superior cooling conditions of the welded specimen compared to all other configurations. The lowest hardness (25%–35% lower than that of the base metal) is observed when welding in an argon atmosphere within a sealed chamber, which is related to the poorest cooling conditions. In other cases of penetration of alloy 7064, the microhardness of the remelted metal is at the level of 70%–90% of the base metal microhardness.

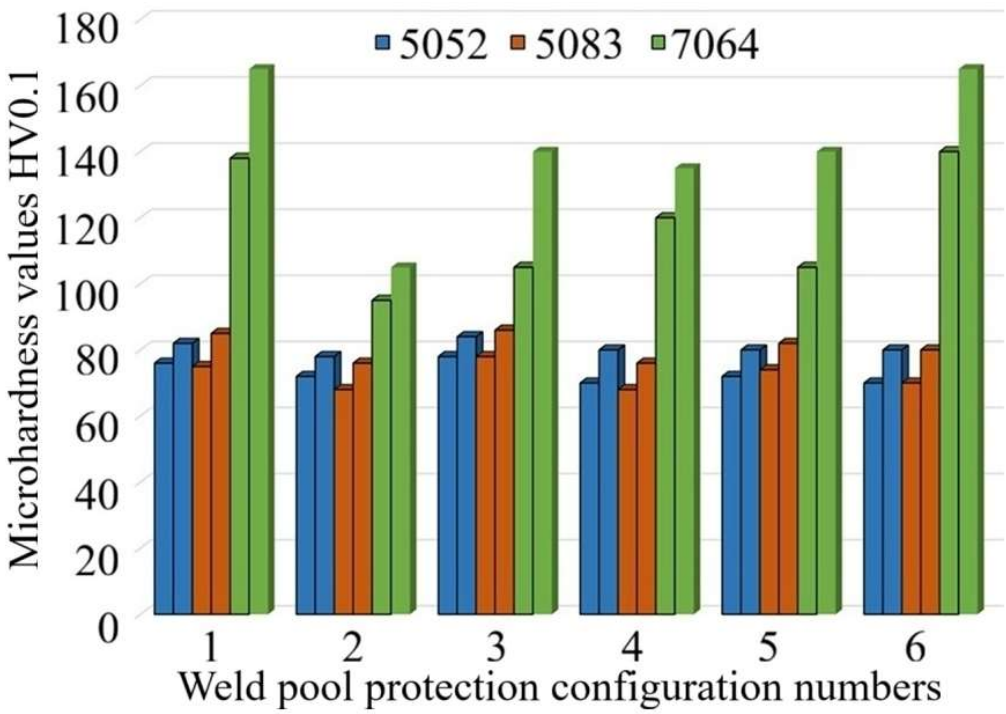

Figure 5. Scatter of microhardness values (HV0.1) of penetrations in samples of aluminum alloys 5052, 5083, and 7064 (δ = 4 mm), obtained under the following gas shielding configurations: 1: in air with local argon shielding of the weld pool; 2: in an argon atmosphere in a sealed chamber; 3: in a chamber in an argon atmosphere with additional argon blowing of the pool; 4: in a chamber in an argon atmosphere at reduced pressure; 5: in a chamber at reduced pressure with additional argon blowing of the pool; and 6: base metal.

The content of alloying elements such as Mg, Zn, and Cu in the remelted metal of the investigated alloys was analyzed using scanning electron microscopy [84,85]. The obtained results are presented in Table 3. The investigation of chemical inhomogeneity in the penetration zones of 5052 and 5083 alloys shows that the distribution of the volatile alloying element magnesium in both the base metal and the weld metal is inhomogeneous. In all cases, a reduction in magnesium content in the weld metal is observed. In the penetration metal of aluminum alloy 5052, the Mg content decreased to 0.63%–1.57% when using shielding gas configuration No. 4. In contrast, when using shielding configurations No. 1, No. 2, and No. 3, the reduction in Mg content in the penetration metal is less than when using configurations No. 4 and No. 5. In turn, the reduction in Mg content observed when employing scheme No. 5 is lower than that observed with scheme No. 4. Thus, lowering the ambient atmosphere pressure facilitates a reduction in magnesium content within the metal of the laser melt pools; however, additional shielding of the weld pool contributes not only to an increased penetration depth but also to a 10%–30% increase in magnesium content compared to melting without shielding.

Table 3. Content of Mg, Zn, and Cu in the metal of laser melt pools produced in samples of 5052, 5083, and 7064 alloys (δ = 5 mm).

Alloy	Gas shielding configuration	Element content in the melted metal (wt.%)/fraction burned off (%)		
		Mg	Zn	Cu
5052	No. 1	2.6/8	-	-
	No. 2	2.23/20	-	-
	No. 3	2.23/20	-	-
	No. 4	1.29/54	-	-
	No. 5	1.57/44	-	-
5083	No. 1	4.6/4	-	-
	No. 2	4.12/14	-	-
	No. 3	4.34/10	-	-
	No. 4	2.38/50	-	-
	No. 5	3.8/20	-	-
7064	No. 1	1.77/34	4.28/39	1.63/14
	No. 2	1.96/27	4.65/34	1.84/3
	No. 3	1.99/26	4.05/42	1.90/0
	No. 4	1.35/50	2.20/68	1.70/11
	No. 5	1.37/49	2.42/65	1.72/9

The most significant magnesium losses during laser penetration of 5052 and 5083 alloys are observed when using weld pool shielding scheme No. 4 (54% and 50%, respectively). The distribution of changes in magnesium content along the depth and width of the laser-melted zone in alloy 5083 with gas shielding configurations No. 4 and No. 5 is presented in Figure 6. It should be noted that such losses in magnesium content in the remelted metal may be critical, as each percentage point of magnesium increases the ultimate tensile strength of the alloy by approximately 30 MPa and the yield strength by approximately 20 MPa [86–89].

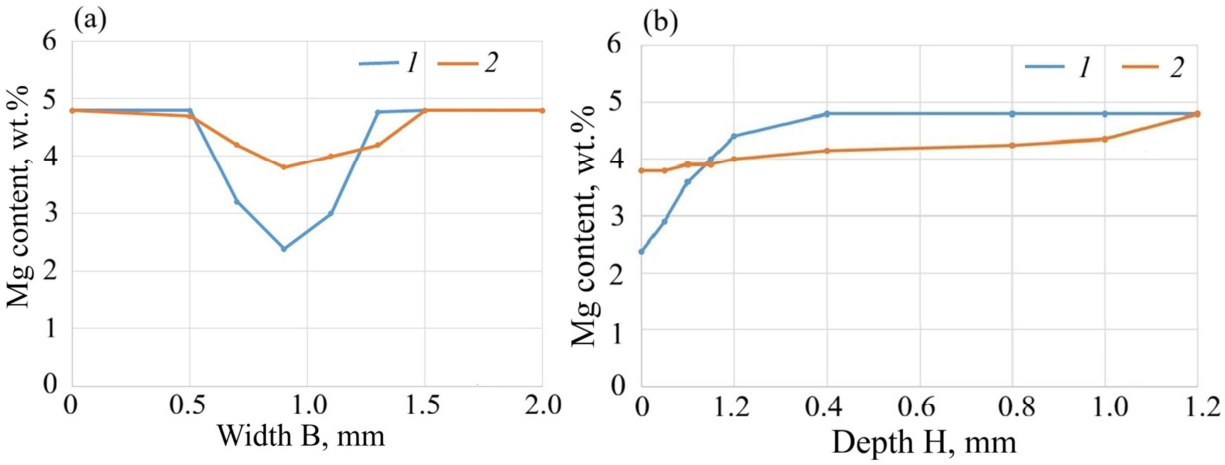

Figure 6. Distribution of changes in Mg content (wt.%) during laser melting in alloy 5083 (δ = 5 mm): (a) along the width B; (b) along the depth H. (*1*: in a chamber with an argon atmosphere at reduced pressure; *2*: in a chamber at reduced pressure with additional purging of the argon bath).

From the perspective of welding in a reduced pressure environment, Al-Zn-Mg-Cu system alloys, particularly alloy 7064, are more promising due to their combination of enhanced mechanical properties. These alloys contain, in addition to magnesium, zinc and copper; the content of these elements in the penetration metal for the 7064 alloy is given in Table 3. Although the content of the studied elements in the weld metal decreases during laser penetration of this alloy, applying shielding to the weld pool also demonstrated somewhat better results. However, due to the high coefficient of linear thermal expansion and the low evaporation temperatures of the light alloying elements (primarily Mg, Zn, and Cu), welding these alloys remains problematic [90,91].

The results of the conducted research established that when employing gas shielding of the weld pool according to schemes No. 1 through No. 4, the melted zones in the Al-Mg (5052, 5083) and Al-Zn-Mg-Cu (7064) systems predominantly exhibit a depth of 0.20–0.23 mm and a width of 0.7–0.8 mm (Table 2). In these melted samples, the heat affected zone (HAZ) is not distinctly pronounced and is characterized by a small size (Figure 7a,b). The shallow depth of laser melting of aluminum alloys is due to the significant (10 mm) focus depth and, consequently, the relatively large diameter of the radiation focusing spot. In this case, a heat conductive mode of melting is observed, characterized by a wider and shallower crystallization bath, which facilitates the vertical growth of crystallites from the fusion boundaries (Figure 7).

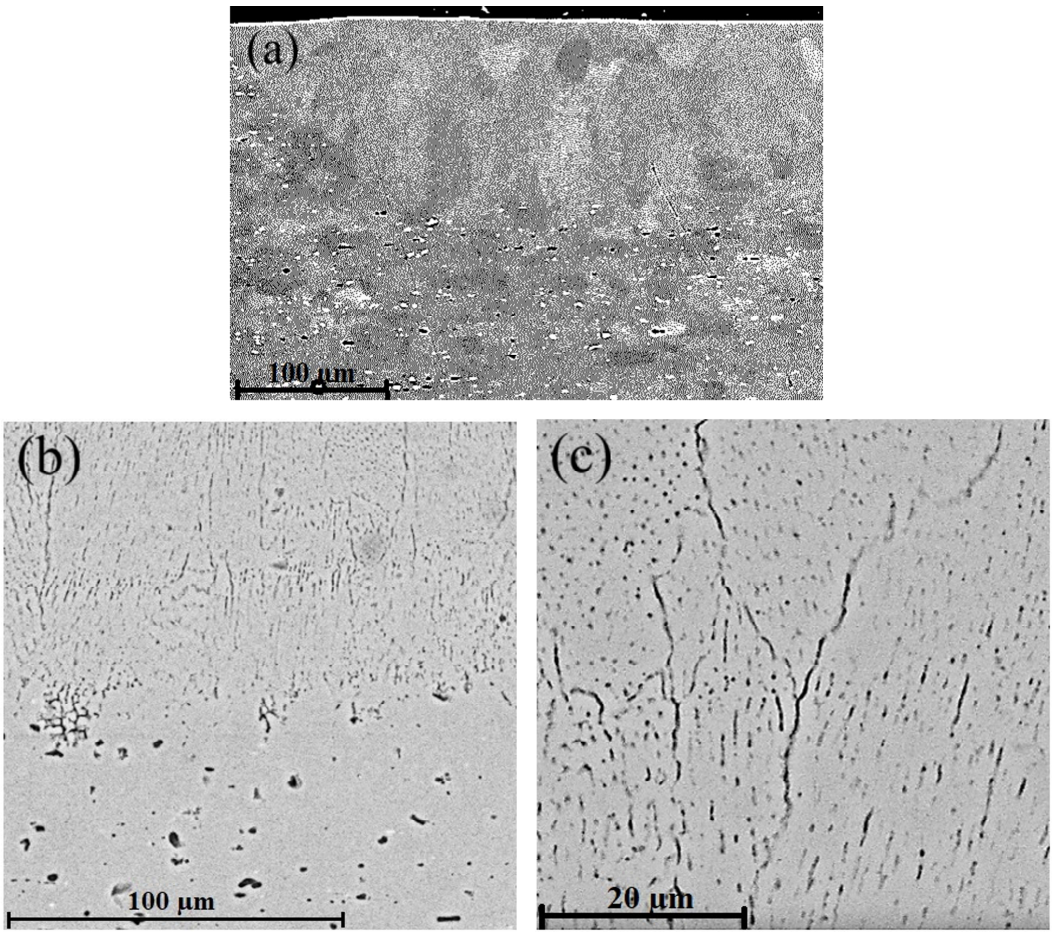

Figure 7. Metal structures laser melt pools of 5052 alloy samples of the Al-Mg system (gas shielding scheme No. 4): (a) melt macrostructure; (b) heat-affected zone; and (c) weld metal.

When using scheme No. 5 for the gas shielding of the weld pool, deep (or dagger-like) laser melting was observed in the samples, characterized by the formation of a vapor-gas channel (keyhole). An example of such melting for the 7064 alloy of the Al-Zn-Mg-Cu system is shown in Figure 8. This type of melting for all the alloys studied is characterized by transcrystallite, counter-directional growth of crystallites from the pool walls at an angle toward the central axis (more precisely, the central zone) of the molten cross-section. Dendrites are oriented from the fusion boundaries toward the solidifying melted metal and grow toward each other from opposite sides of the surfaces toward the fusion axis, resulting in a characteristic structure with ordered crystalline grains. Consequently, in the central part of the weld, a mixture of equiaxed and oriented dendrites is observed. The formation of an impurity-enriched liquid in the axial zone at the junction of crystallites under such bath geometry may lead to the development of a weakened interface between columnar crystals, which could hypothetically facilitate the formation of cracks under welding-induced deformations.

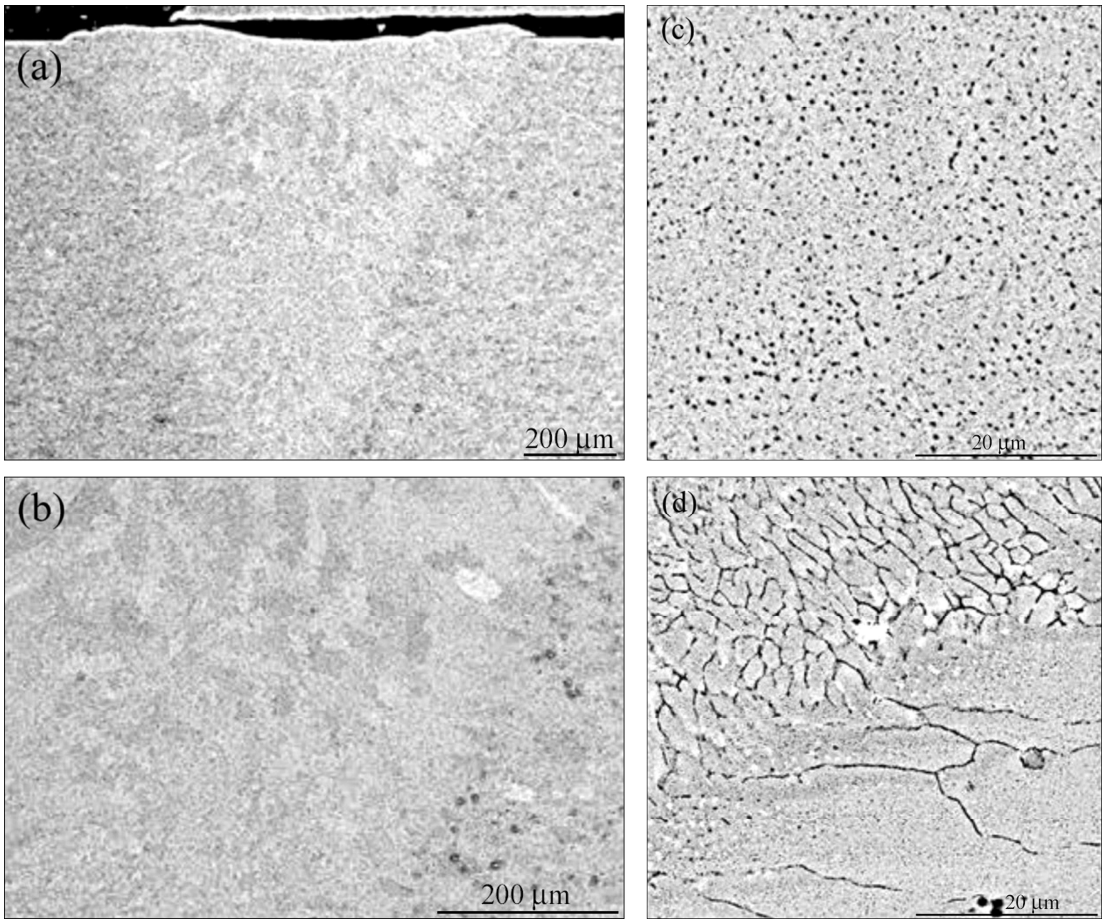

Figure 8. Structures of the metal in the laser melt pools of 7064 alloy samples from the Al-Zn-Mg-Cu system (gas shielding configuration No. 5): (a) and (b): melt macrostructure; (c): weld metal; and (d): heat-affected zone.

Microstructural analysis of the melt pools in 5052 and 5083 alloy samples of the Al-Mg alloying system demonstrate that, in both the base metal and the weld metal, in addition to the α-solid solution of magnesium in aluminum, double and more complex β-phases (Mg_2Al_3 or Mg_5Al_3) are also present.

These phases are distributed within the melted metal as fine eutectic precipitates located between dendrite arms. In the 7063 alloy of the Al-Zn-Mg-Cu system, zinc and magnesium exhibit significant solubility at elevated temperatures (400 °C) and minimal solubility at lower temperatures (below 200 °C). The primary strengthening phase in the 7064 alloy is the T-phase ($Al_2Mg_3Zn_3$). An addition of approximately 2% Cu is present, which enhances corrosion resistance.

The phase precipitates in the penetration metal are finely dispersed, and the fusion boundaries exhibit no signs of overheating. Continuous chains of precipitates are also observed outside the grains in the HAZ, directly along the fusion boundaries. The fusion zones themselves are very narrow, with a fine-grained structure, and represent a continuous transition of grains from the base metal to the weld metal crystallites. It should be noted that the deformation texture of the base metal is preserved identically right up to the fusion zones (Figures 7 and 8), while no grain recrystallization is observed in the heat-affected zones.

5. Conclusions

1. The influence of argon gas shielding configurations of the weld pool on the melting behavior of Al-Mg and Al-Zn-Mg-Cu aluminum alloy samples with a thickness of 4–5 mm under fiber laser irradiation at 900 W power and a linear energy input of 100–130 J/mm was investigated. It was determined that when using local argon shielding in an open atmosphere, as well as a shielding environment in a controlled atmosphere chamber at normal (1.0–1.05 MPa) and reduced (170–190 Pa) pressure, partial penetration melting of plate-shaped samples occurs in a heat conductive regime to a depth of 0.20–0.23 mm. However, when the melt pool is purged with argon at a flow rate of 5–10 L/min in a chamber with reduced pressure of 170–190 Pa, a transition to deep (keyhole) melting is observed, characterized by a fivefold increase in penetration depth and a corresponding fivefold decrease in the specific melting energy density (from 8900–9000 to 1800 J/mm^2).

2. It has been established that during laser penetration in the heat conduction regime in air with local argon shielding, the Mg content in the remelted metal decreases by 4%–8% for Al-Mg alloys and the content of Mg, Zn, and Cu decreases by 15%–40% for Al-Zn-Mg-Cu alloys. The microhardness of the metal in the penetrations is close to that of the base metal. In the remelted metal, Al_2O_3 oxides are observed, constituting approximately 3% of the penetration cross-sectional area.

3. When employing a surrounding protective atmosphere of argon at a pressure of 1.05 MPa, the fraction of oxide inclusions constitutes 1.5%–2.0% of the cross-sectional area of the melt. Furthermore, the content of alloying elements decreases, amounting to 74%–90% for Mg, 66% for Zn, and 97% for Cu, while the microhardness of the melt metal is reduced by 10%–35% compared to the base metal. With additional argon blowing of the melt bath at a flow rate of 5–10 L/min, the content of alloying elements is 73–86% for Mg, 58% for Zn, and 100% for Cu, and the microhardness of the melt metal ranges from a 15% decrease to a 5% increase relative to the base metal.

4. It was determined that reducing the pressure of the surrounding shielding atmosphere to 170–190 Pa leads to a decrease in the proportion of oxide inclusions to 1.5% and below in the melting cross-section. However, this also results in a reduction in the content of alloying elements, specifically Mg to 46%–50%, Zn to 32%, and Cu to 89%. Additionally, the microhardness of the metal in the melted regions decreases by 10%–30% compared to the base metal. Argon shielding of the weld pool at flow rates of 5–10 L/min under reduced pressure of 170–190 Pa facilitates an increase in the

proportion of alloying elements in the remelted metal to 51%–80% for Mg, 35% for Zn, and 91% for Cu, as well as a 5%–10% reduction in the microhardness loss effect.

5. It has been established that laser melting of the investigated alloys in heat conductivity mode results in the formation of remelted metal tracks with depths of 0.20–0.23 mm and widths of 0.7–0.8 mm, which, during weld pool crystallization, promote the vertical growth of crystallites from the fusion boundary and the segregation of low-melting constituents to the surface. In the case of laser melting in the deep (keyhole) mode, the tracks of remelted metal in cross-section had both depth and width of 1.0 mm, exhibiting transcrystalline counter-growth of crystallites from the pool walls at an angle toward the central melting zone, with the segregation of low-melting constituents into the central melting zone.

6. It has been established that the optical homogeneity of the surface of welded aluminum alloys contributes to the improvement of the formation of seams and penetrations by stabilizing the absorption of laser radiation. It is proposed to achieve such stabilization by preliminary chemical etching of the welded edges instead of scraping them, which allows to eliminate the ingress of oxide film residues into the metal, which significantly increase the absorption of radiation.

Use of AI tools declaration

The authors declare they have not used Artificial Intelligence (AI) tools in the creation of this article.

Acknowledgments

The research was funded within the following programs: the GDAS'Project of Science and Technology Development (2020GDASYL-20200301001); National Key R&D Program of China (2020YFE0205300).

Author contributions

V. Korzhyk, O. Babych: general research management, work ideology; X. Wang, V. Khaskin: research methodology, conclusions; S. Peleshenko, A. Chaika, A. Aloshyn: conducting technological and metallographic studies; Y. Zhao, Guirong, Y. Hu: processing of results, writing the article.

Conflict of interest

The authors declare no conflict of interest.

References

1. Li SS, Yue X, Li QY, et al. (2023) Development and applications of aluminum alloys for aerospace industry. *J Mater Res Technol* 27: 944–983. https://doi.org/10.1016/j.jmrt.2023.09.274
2. Soni R, Verma R, Garg RK, et al. (2024) A critical review of recent advances in the aerospace materials. *Mater Today Proc* 113: 180–184. https://doi.org/10.1016/j.matpr.2023.08.108

3. Zhang Y, Shan H, Li Y, et al. (2017) Effects of the oxide film on the spot joining of aluminum alloy sheets: A comparative study between resistance spot welding and resistance spot clinching. *Int J Adv Manuf Technol* 92: 4231–4240. https://doi.org/10.1007/s00170-017-0387-x
4. Zlatanovic LD, Bergmann PJ, Balos S, et. al. (2023) Effect of surface oxide layers in solid-state welding of aluminium alloys—Review. *Sci Technol Weld Join* 28: 331–351. https://doi.org/10.1080/13621718.2023.2165603
5. Silva DCC, Scotti A (2016) Using either Mean or RMS values to represent current in modeling of arc welding bead geometries. *J Mater Process Technol* 240: 382–387. https://doi.org/10.1016/j.jmatprotec.2016.10.008
6. Korzhik VN (1992) Theoretical analysis of the conditions required for rendering metallic alloys amorphous during gas-thermal spraying. III. Transformations in the amorphous layer during the growth process of the coating. *Powder Metall Met Ceram* 31: 943–948. https://doi.org/10.1007/BF00797621
7. Wu B, Krivtsun IV (2019) Processes of nonconsumable electrode welding with welding current modulation (Review). Part 1. Peculiarities of burning of nonstationary arcs with refractory cathode. *Paton Weld J* 11: 23–32. https://doi.org/10.15407/tpwj2019.11.05
8. Prokopov VG, Fialko NM, Sherenkovskaya GP, et al. (1993) Effect of the coating porosity on the processes of heat transfer under, gas-thermal atomization. *Powder Metall Met Ceram* 32: 118–121. https://doi.org/10.1007/BF00560034
9. Wu B, Krivtsun IV (2019) Processes of nonconsumable electrode welding with welding current modulation (Review). Part II. Effects of arc impact on the metal being welded. *Paton Weld J* 12: 11–23. https://doi.org/10.15407/tpwj2019.12.02
10. Fialko N, Prokopov V, Meranova N, et al. (1993) Thermal physics of gas thermal coatings formation processes. State of investigations. *Fiz Khim Obrab Mater* 4: 83–93. Available from: https://www.scopus.com/pages/publications/0027635013?inward=.
11. Fialko NM, Prokopov VG, Meranova N, et al. (1994) Temperature conditions of particle-substrate systems in a gas-thermal deposition process. *Fiz Khim Obrab Mater* 2: 59–67. Available from: https://www.scopus.com/pages/publications/0028385421?origin=resultslist.
12. Verma RP, Pandey KN, Andras K, et al. (2023) Difficulties and redressal in joining of aluminium alloys by GMA and GTA welding: a review. *J Mater Res Technol* 23: 2576–2586. https://doi.org/10.1016/j.jmrt.2023.01.183
13. Wei Y, Chen Y, Niu R, et al. (2022) Study on the Thermal Conductivity of Cu/Al joints with different interfacial microstructures. *Adv Mater Sci Eng* 2022: 7040685. https://doi.org/10.1155/2022/7040685
14. Kostrivas A, Lippold JC (1999) Weldability of Li-bearing aluminium alloys. *Int Mater Rev* 44: 217–237. https://doi.org/10.1179/095066099101528289
15. Verma RP, Lila MK (2021) A short review on aluminium alloys and welding in structural applications. *Mater Today Proc* 46: 10687–10691. https://doi.org/10.1016/j.matpr.2021.01.447
16. Sydorets V, Korzhyk V, Khaskin V, et al. (2017) On the thermal and electrical characteristics of the hybrid plasma-MIG welding process. *Mater Sci Forum* 906: 63–71. https://doi.org/10.4028/www.scientific.net/MSF.906.63

17. Zhang ZH, Dong SY, Wang YJ, et al. (2016) Study on microstructures and mechanical properties of super narrow gap joints of thick and high strength aluminum alloy plates welded by fiber laser. *Int J Adv Manuf Technol* 82: 99–109. https://doi.org/10.1007/s00170-015-7334-5
18. Kvasnytskyi V, Korzhyk V, Lahodzinkyi I, et al. (2020) Creation of volumetric products using additive arc cladding with compact and powder filler materials. 2020 IEEE 10th International Conference Nanomaterials: Applications & Properties (NAP), Sumy, Ukraine. https://doi.org/10.1109/NAP51477.2020.9309696
19. Li JG, Wang SQ (2017) Distortion caused by residual stresses in machining aeronautical aluminumalloy parts: Recent advances. *Int J Adv Manuf Technol* 89: 997–1012. https://doi.org/10.1007/s00170-016-9066-6
20. Han J, Shi Y, Guo JC, et al. (2023) Porosity inhibition of aluminum alloy by power-modulated laser welding and mechanism analysis. *J Manuf Proc* 102: 827–83. https://doi.org/10.1016/j.jmapro.2023.08.001
21. Sydorets V, Korzhyk V, Khaskin V, et al. (2017) Electrical characteristics of the equipment for the hybrid plasma-MIG welding. 2017 IEEE 58th International Scientific Conference on Power and Electrical Engineering of Riga Technical University (RTUCON), Riga, Latvia, 1–6. https://doi.org/10.1109/RTUCON.2017.8124811
22. Olabode M, Kah P, Martikainen J (2013) Aluminium alloys welding processes: Challenges, joint types and process selection. *Proc Inst Mech Eng Pt B J Eng Manuf* 227: 1129–1137. https://doi.org/10.1177/0954405413484015
23. Chen BQ, Liu K, Xu S (2024) Recent advances in aluminum welding for marine structures. *J Mar Sci Eng* 12: 1539. https://doi.org/10.3390/jmse12091539
24. Urminský J, Marônek M, Bárta J, et. al. (2020) Electron beam welding of aluminium alloy AW2099. *Mater Sci Forum* 994: 28–35. https://doi.org/10.4028/www.scientific.net/MSF.994.28
25. Jiang F, Li W, Xu B, et al. (2024) Variable polarity plasma arc welding: Process development and its recent developments of detecting, modeling, and controlling. *J Manuf Proc* 114: 1–17. https://doi.org/10.1016/j.jmapro.2024.01.078
26. Rakhi K, Kang S, Shin J (2023) Hot-cracking mechanism of laser welding of aluminum alloy 6061 in lap joint configuration. *Materials* 16: 6426. https://doi.org/10.3390/ma16196426
27. Idriss M, Mirakhorli F, Desrochers A, et al. (2022) Overlap laser welding of 5052-H36 aluminum alloy: Experimental investigation of process parameters and mechanical designs. *Int J Adv Manuf Technol* 119: 7653–7667. https://doi.org/10.1007/s00170-022-08783-3
28. Liu RP, Dong ZJ, Pan YM (2006) Solidification crack susceptibility of aluminum alloy weld metals. *Trans Nonferrous Met Soc China* 16: 110–116. https://doi.org/10.1016/S1003-6326(06)60019-8
29. Pamarthi VV, Sun T, Das A, et al. (2023) Tailoring the weld microstructure to prevent solidification cracking in remote laser welding of AA6005 aluminium alloys using adjustable ringmode beam. *J Mater Res Technol* 25: 7154–7168. https://doi.org/10.1016/j.jmrt.2023.07.154
30. Al-Badour F, Bawagnih AH, Ali A, et al. (2025) Surface cracks repair in AA6061-T6 aluminum alloys using friction stir processing. *J Adv Join Process* 12: 100340. https://doi.org/10.1016/j.jajp.2025.100340

31. Yang X, Chong X, Chen M, et al. (2025) Laser welding crack suppression of ultra-high strength aluminum alloys based on filled slats. *J Alloys Metallurg Syst* 11: 100202. https://doi.org/10.1016/j.jalmes.2025.100202
32. Han X, Sun X, Li G, et al. (2021) A repair method for damage in aluminum alloy structures with the cold spray process. *Materials* 14: 6957. https://doi.org/10.3390/ma14226957
33. Dehghanpour S, Nezamabadi A, Attar M, et al. (2019) Repairing cracked aluminum plates by aluminum patch using diffusion method. *J Mech Sci Technol* 33: 4735–4743. https://doi.org/10.1007/s12206-019-0914-9
34. Jin J, Geng S, Shu L, et al. (2024) High-strength and crack-free welding of 2024 aluminium alloy via Zr-core-Al-shell wire. *Nat Commun* 15: 1748. https://doi.org/10.1038/s41467-024-45660-x
35. Renna G, Leo P, Casalino G, et al. (2018) Repairing 2024 aluminum alloy via electrospark deposition process: A feasibility study. *Adv Mater Sci Eng* 218: 8563054. https://doi.org/10.1155/2018/8563054
36. Saha P, Ghosh A, Das K, et al. (2024) Laser welding of aluminum alloys, In: Kunar S, Chatterjee P, *Laser-Assisted Machining*, Beverly: Scrivener Publishing LLC, 207–225. https://doi.org/10.1002/9781394214655.ch12
37. Kvasnová P, Novák D, Novák V (2017) Laser welding of aluminium alloys. *Manuf Technol* 17: 892–898. https://doi.org/10.21062/ujep/x.2017/a/1213-2489/MT/17/6/892
38. Alfieria V, Caiazzoa F, Sergi V (2015) Autogenous laser welding of AA 2024 aluminium alloy: Process issues and bead features. *Procedia CIRP* 33: 406–411. https://doi.org/10.1016/j.procir.2015.06.094
39. Schneider A, Avilov V, Gumenyuk A, et al. (2013) Laser beam welding of aluminum alloys under the influence of an electromagnetic field. *Phys Procedia* 41: 4–11. https://doi.org/10.1016/j.phpro.2013.03.045
40. Murakawa H (2013) 13—Residual stress and distortion in laser welding, In: Katayama S, *Handbook of Laser Welding Technologies*, Cambridge: Woodhead Publishing, 374–400e. https://doi.org/10.1533/9780857098771.2.374
41. Ya M, Marquette P, Belahcene F, et al. (2004) Residual stresses in laser welded aluminium plate by use of ultrasonic and optical methods. *Mater Sci Eng A* 382: 257–264. https://doi.org/10.1016/j.msea.2004.05.020
42. Mascenik J, Pavlenko S (2020) Determination of stress and deformation during laser welding of aluminium alloys with the pc support. *MM Sci J* 4: 4104–4107. http://doi.org/10.17973/MMSJ.2020_11_2020037
43. Wang Z, Yang P, Liao W, et al. (2025) Stresses numerical analysis of oscillating laser welding in aluminum alloys based on the equivalent fluid–structure interactions model. *Opt Laser Technol* 191: 113365. https://doi.org/10.1016/j.optlastec.2025.113365
44. Tang J, Hu M, Su J, et al. (2025) Deformation control of adjustable-ring-mode (ARM) laser welding for aluminum alloys. *Materials* 18: 860. https://doi.org/10.3390/ma18040860
45. Chen X, Tang S, Xie W, et al. (2023) Numerical simulation and experimental study of residual stress in dissimilar aluminum alloy laser composite welding. *Proc Inst Mech Eng Part L J Mater Des Appl* 238: 1155–1163. https://doi.org/10.1177/14644207231212976
46. Zhao H, White DR, DebRoy T (1999) Current issues and problems in laser welding of automotive aluminium alloys. *Int Mater Rev* 44: 238–266. https://doi.org/10.1179/095066099101528298

47. Wallerstein D, Salminen A, Lusquiños F, et al. (2021) Recent developments in laser welding of aluminum alloys to steel. *Metals* 11: 622. https://doi.org/10.3390/met11040622
48. Dada M, Popoola P (2024) Recent advances in joining technologies of aluminum alloys: A review. *Discov Mater* 4: 86. https://doi.org/10.1007/s43939-024-00155-w
49. Chen C, Li L, Zhang M, et al. (2024) Effects of different surface treatment methods on laser welding of aluminum alloy and glass. *Coatings* 14: 1318. https://doi.org/10.3390/coatings14101318
50. Dausinger F (2000) Laser welding of aluminum alloys: From fundamental investigation to industrial application. *Proc SPIE–Int Soc Opt Eng* 3888. https://doi.org/10.1117/12.377044
51. Karami S, Yousefieh M, Naffakh-Moosavy H (2025) The effect of laser welding parameters on mechanical properties and microstructure evolution of multi-layered 6061 aluminum alloy. *J Adv Join Process* 11: 100275. https://doi.org/10.1016/j.jajp.2024.100275
52. Mu H, Luo S, Wang L, et al. (2024) Microstructure and mechanical properties of aluminum alloy laser welded joint assisted by alternating magnetic field. *J Mater Res Technol* 33: 6842–6852. https://doi.org/10.1016/j.jmrt.2024.11.054
53. Castro D, Illade J, Gonzalez N, et al. (2025) The advanced real-time monitoring of new welding processes in the aircraft industry. *Eng Proc* 90: 7. https://doi.org/10.3390/engproc2025090007
54. Freeman R (2012) 1—New welding techniques for aerospace engineering, In: Chaturvedi MC, *Welding and Joining of Aerospace Materials*, Cambridge: Woodhead Publishing, 3–24. https://doi.org/10.1533/9780857095169.1.1
55. Giampieri A, Ma Z, Ling-Chin J, et al. (2022) An overview of solutions for airborne viral transmission reduction related to HVAC systems including liquid desiccant air-scrubbing. *Energy* 244: 122709. https://doi.org/10.1016/j.energy.2021.122709
56. Davis JR (1998) Chemical compositions and international designations for aluminum alloys, In: Davis JR, *Metals Handbook Desk Edition*, 2 Eds., Ohio: ASM International, 436. https://doi.org/10.31399/asm.hb.mhde2.a0003123
57. Novianto E, Iswanto PT, Mudjijana M (2018) The effects of welding current and purging gas on mechanical properties and microstructure of tungsten inert gas welded aluminum alloy 5083 H116. *MATEC Web Conf* 197: 12007. https://doi.org/10.1051/matecconf/201819712007
58. Şahin EI, Emek M, Ibrahim JEFM (2023) *Instrumental Measurements Laboratory*, Istanbul: Iksad Publishing House. Available from: https://iksadyayinevi.com/wp-content/uploads/2023/05/INSTRUMENTAL-MEASUREMENTS-LABORATORY-1.pdf.
59. Fialko N, Dinzhos R, Sherenkovskaya G, et al. (2022) Influence on the thermophysical properties of nanocomposites of the duration of mixing of components in the polymer melt. *East-Eur J Enterp Technol* 2: 25–30. https://doi.org/10.15587/1729-4061.2022.255830
60. Kvasnytskyi V, Korzhyk V, Kvasnytskyi V, et al. (2020) Designing brazing filler metal for heat-resistant alloys based on Ni3Al intermetallide. *East-Eur J Enterp Technol* 6: 6–19. https://doi.org/10.15587/1729-4061.2020.217819
61. Skorokhod AZ, Sviridova IS, Korzhik VN (1995) The effect of mechanical pretreatment of polyethylene terephthalate powder on the structural and mechanical properties of coatings made from it. *Mech Compos Mater* 30: 328–334. https://doi.org/10.1007/BF00634755

62. Mao D, Xie Y, Meng X, et al. (2024) Strength-ductility materials by engineering a coherent interface at in coherent precipitates. *Mater Horiz* 11: 3408–3419. https://doi.org/10.1039/D4MH00139G
63. Gu Y, Zhang W, Xu Y, et al. (2022) Stress-assisted corrosion behaviour of Hastelloy N in FLiNaK molten salt environment. *npj Mater Degrad* 6: 90. https://doi.org/10.1038/s41529-022-00300-x/
64. Borisov YuS, Kunitskii YuA, Korzhik VN, et al. (1986) Structure and some physical properties of plasma-sprayed coatings of the nickel boride Ni_3B. *Powder Metall Met Ceram* 25: 966–969. https://doi.org/10.1007/BF00797102
65. Adamiec J, Pfeifer T, Rykała J (2011) Modern methods of aluminum alloys welding. *Solid State Phenom* 176: 35–38. https://doi.org/10.4028/www.scientific.net/ssp.176.35
66. Fialko N, Dinzhos R, Sherenkovskii J, et al. (2021) Establishment of regularities of influence on the specific heat capacity and thermal diffusivity of polymer nanocomposites of a complex of defining parameters. *East-Eur J Enterp Technol* 114: 34–39. https://doi.org/10.15587/1729-4061.2021.245274
67. Borisov Y, Korzhyk V (1998) Internal stresses in plasma coatings with an amorphous structure. *ITSC Proc* 1: 693–697. https://doi.org/10.31399/asm.cp.itsc1998p0693
68. Ain MQU, Naik DK, Rajendran DK, et al. (2025) Comprehensive analysis of experimental studies in cold metal transfer welding. *Discov Appl Sci* 7: 590. https://doi.org/10.1007/s42452-025-07065-3
69. Borisov Y, Korzhyk V, Revo S (1998) Electric and magnetic properties of thermal spray coatings with an amorphous structure. *ITSC Proc* 1: 687–691. https://doi.org/10.31399/asm.cp.itsc1998p0687
70. Wang Z, Zhang B, Zhang W, et al. (2025) Effect of laser line energy on the microstructure, mechanical properties and corrosion resistance of Q355B welded by local dry underwater laser welding. *Opt Laser Technol* 183: 112370. https://doi.org/10.1016/j.optlastec.2024.112370
71. Giudice F, Sili A (2023) Validation of a theoretical model for laser welding thermal field by multi-physics numerical simulation. *Metals* 13: 2020. https://doi.org/10.3390/met13122020
72. Frederic C, Janin F, Hamadou M, et al. (2002) Deep-penetration laser welding with Nd:YAG laser combination up to 11kW laser power. *Proc SPIE–Int Soc Opt Eng* 4831. https://doi.org/10.1117/12.486494
73. Zou JL, He Y, Wu SK, et al. (2015) Experimental and theoretical characterization of deep penetration welding threshold induced by 1-μm laser. *Appl Surf Sci* 357B: 1522–1527. https://doi.org/10.1016/j.apsusc.2015.09.198
74. Katayama S, Yohei A, Mizutani M, et al. (2011) Development of deep penetration welding technology with high brightness laser under vacuum. *Phys Procedia* 12: 75–80. https://doi.org/10.1016/j.phpro.2011.03.010
75. Ai Y, Zhang Y, Han S, et al. (2025) Numerical investigation on the molten pool and keyhole dynamic behaviors and weld microstructure in laser-induction hybrid welding of stainless steel. *Int J Heat Mass Transf* 245: 126988. https://doi.org/10.1016/j.ijheatmasstransfer.2025.126988
76. Ai Y, Ye C, Liu J, et al. (2025) Study on the evolution processes of keyhole and melt pool in different laser welding methods for dissimilar materials based on a novel numerical model. *Int Commun Heat Mass Transf* 163: 108629. https://doi.org/10.1016/j.icheatmasstransfer.2025.108629

77. Budde L, Biester K, Huse M, et al. (2022) Empirical model for the description of weld seam geometry in coaxial laser hot-wire deposition welding processes with different steel wires. *Lasers Manuf Mater Process* 9: 193–213. https://doi.org/10.1007/s40516-022-00170-w
78. Ren Z, Fu G, Liu F, et al. (2024) Elucidation of laser irradiation behaviors associated with the keyhole dynamics during laser powder bed fusion. *J Mater Res Technol* 32: 1672–1682. https://doi.org/10.1016/j.jmrt.2024.08.019
79. Kaufmann F, Maier A, Schrauder J, et al. (2024) Influence of laser beam intensity distribution on keyhole geometry and process stability using green laser radiation, In: Silva FJG, Pereira AB, Campilho RDSG, *Flexible Automation and Intelligent Manufacturing: Establishing Bridges for More Sustainable Manufacturing Systems. FAIM 2023. Lecture Notes in Mechanical Engineering*, Cham: Springer, 216–227. https://doi.org/10.1007/978-3-031-38241-3_25
80. Caruso S, Saffioti MR, Rotella G (2025) Modelling microstructural alterations and the formation of keyhole-mode melting on Ti6Al4V during single-pass laser ablation. *Int J Adv Manuf Technol* 139: 4085–4095. https://doi.org/10.1007/s00170-025-16161-y
81. ISO 13919-2:2001 Welding–Electron and laser-beam welded joints–Guidance on quality levels for imperfections–Part 2: Aluminium and its weldable alloys. Available from: https://www.iso.org/ru/standard/75515.html.
82. Blaško P, Petrík J, Šolc M, et al. (2025) The effect of aluminum deformation conditions on microhardness and indentation size effect characteristics. *Crystals* 15: 252. https://doi.org/10.3390/cryst15030252
83. Petrík J (2016) On the load dependence of micro-hardness measurements: analysis of data by different models and evaluation of measurement errors. *Arch Metall Mater* 61: 1819–1824. https://doi.org/10.1515/amm-2016-0294
84. Tillová E, Chalupová M, Kuchariková L, et al. (2013) Scanning electron microscopy identification of intermetallic phases in Al-Si cast alloys. *Acta Metall Slovaca* 3: 196–201. https://doi.org/10.12776/amsc.v3i0.127
85. Vernon-Parry KD (2000) Scanning electron microscopy: An introduction. *III-Vs Review* 13: 40–44. https://doi.org/10.1016/S0961-1290(00)80006-X
86. Mackenzie SD (2018) Metallurgy of heat treatable aluminum alloys, In: Anderson K, Weritz J, Kaufman JG, *Aluminum Science and Technology*, Ohio: ASM International, 411–437. https://doi.org/10.31399/asm.hb.v02a.a0006509
87. Siddesh KNM, Dhruthi, Pramod GK, et al. (2022) A critical review on heat treatment of aluminium alloys. *Mater Today Proc* 58: 71–79. https://doi.org/10.1016/j.matpr.2021.12.586
88. Carta M, Aydi L, Buonadonna P, et al. (2024) Effect of post heat treatment on microstructure and mechanical properties of hot-rolled AA2017 aluminum alloy. *Heliyon* 10: e40922. https://doi.org/10.1016/j.heliyon.2024.e40922
89. Md Sujon A, Md Sayed A, Md Shariful I, et al. (2023) Experimental study on the effects of three alloying elements on the mechanical, corrosion and microstructural properties of aluminum alloys. *Res Mater* 20: 100485. https://doi.org/10.1016/j.rinma.2023.100485
90. Radkovský F, Gawronová M, Válková N, et al. (2022) Determination of linear expansion of AlSi10Mg aluminium alloy depending on external conditions during solidification. *Heliyon* 8: e11363. https://doi.org/10.1016/j.heliyon.2022.e11363

91. Feng X, Xu Y, Shi Y, et al. (2024) Effects of microstructure and morphological distribution on hydrogen-embrittlement sensitivity of Ti-6Al-4V alloy welded joint. *Int J Hydrog Energy* 50: 361–371. https://doi.org/10.1016/j.ijhydene.2023.11.041

AIMS Press

© 2025 the Author(s), licensee AIMS Press. This is an open access article distributed under the terms of the Creative Commons Attribution License (http://creativecommons.org/licenses/by/4.0)